AIP | Applied Physics Letters

Nonlinear response of an ultracompact waveguide Fabry-Pérot resonator

S. Sederberg and A. Y. Elezzabi

Citation: Applied Physics Letters **102**, 011133 (2013); doi: 10.1063/1.4775368
View online: http://dx.doi.org/10.1063/1.4775368
View Table of Contents: http://scitation.aip.org/content/aip/journal/apl/102/1?ver=pdfcov
Published by the AIP Publishing

Nonlinear response of an ultracompact waveguide Fabry-Pérot resonator

S. Sederberg and A. Y. Elezzabi
Ultrafast Optics and Nanophotonics Laboratory, Department of Electrical and Computer Engineering, University of Alberta, Edmonton T6G 2V4, Canada

(Received 23 November 2012; accepted 20 December 2012; published online 11 January 2013)

We experimentally demonstrate active tuning of an ultracompact silicon-on-insulator trapezoid Fabry-Pérot resonator having a volume of 5.31 μm^3. We show that the ultrafast nonlinear dynamics arising from two-photon and free-carrier absorption can be used to achieve a signal attenuation of 66% in the device, and the changes in the steady-state resonant properties of the device resulting from the thermo-optic effect induce a large red-shift in its resonance of $\Delta\lambda = 7.57$ nm. It is envisaged that the insight gained from this class of device will be valuable in the integrated optics community as ultrafast modulators, and switches are designed to occupy smaller volumes. © *2013 American Institute of Physics*. [http://dx.doi.org/10.1063/1.4775368]

Silicon-on-insulator (SOI) waveguides have enabled rapid development of ultracompact photonic devices with a variety of functionalities including routing, modulating, filtering, and buffering telecommunications signals.[1] For low-intensity continuous-wave (CW) radiation in the telecommunications spectral band (1260 nm $\leq \lambda \leq$ 1675 nm), bulk silicon is virtually lossless. As such, propagation losses in SOI waveguides are dominated by sidewall roughness resulting from fabrication. At high optical intensities, the relatively large $\chi^{(3)}$ nonlinearity in silicon ($n_2 = 3.2 \times 10^{-14}$ cm^2/W) provides a means for ultrafast active control of SOI-based nonlinear photonic devices.[2] Nonlinear optical process, such as four-wave mixing, self-phase modulation, cross-phase modulation, Raman amplification, two-photon absorption (TPA), and free-carrier absorption (FCA) and dispersion have all been exploited in SOI waveguide devices for a variety of applications.[3] Along with its high third-order optical nonlinearity, silicon exhibits a large thermo-optic coefficient ($\Delta n/\Delta T = 1.86 \times 10^{-4}$/K, where Δn and ΔT are changes in the refractive index and temperature, respectively),[4] which has been used to demonstrate thermal switching devices.[5–13]

As with any chip-scale technology, it is essential that the footprint of a photonic device be reduced to as small an area as possible. In the case of ultrafast all-optical modulators working on the principle of TPA and FCA, a high density of free-carriers can be generated in the small volume of the device's waveguide core. Due to silicon's indirect bandgap, nonradiative recombination is the dominant free-carrier relaxation pathway, which occurs over a timescale of hundreds of picoseconds to several nanoseconds in nanoscale SOI waveguides.[3] As the free-carriers relax, thermal energy is deposited directly in the device's waveguide core, modifying the silicon's refractive index. The thermo-optic effect becomes more pronounced for nanoscale Si-based resonant or interference devices where a slight refractive index change shifts the device's resonant wavelength. Although there have been extensive efforts to demonstrate ultrafast modulation devices based on TPA and FCA[14–18] and to demonstrate slower tuning devices based on the thermo-optic effect,[5–13] these investigations have not been interlinked. Most ultrafast modulation experiments are performed in long device lengths ranging from 100 $\mu m \leq L \leq 10$ cm, where the large volume of the device acts to moderate the temperature of the device and thermo-optic effects are minimal. However, for compact, isolated SOI photonic devices, the interplay between both TPA and FCA, and the thermo-optic effect are significant and can influence the operational characteristics.

In this Letter, we demonstrate an ultracompact SOI trapezoid Fabry-Pérot resonator (TFPR) having a volume of only 5.31 μm^3. We show that the ultrafast nonlinear dynamics arising from TPA and FCA can be used to achieve a signal attenuation of 66% in the TFPR, and the changes in the steady-state resonant properties of the device resulting from the thermo-optic effect induce a large red-shift in the TFPR resonance of $\Delta\lambda = 7.57$ nm.

We consider SOI TFPR waveguides with cross-sectional dimensions, $w \times h = 2.0\ \mu m \times 0.34\ \mu m$, and excite the quasi-transverse-magnetic mode. Ten short TFPRs, having lengths ranging from 7.80 $\mu m \leq L \leq 115\ \mu m$ are studied. An on-axis end-fire coupling and detection scheme would give rise to considerable scattered radiation from the excitation being coupled to the detector when the device length is reduced to less than a few tens of micrometers. In order to circumvent this issue, the TFPR end-facets are cleaved perpendicular to one another, as shown in Fig. 1. This configuration ensures that any radiation that is not coupled to the device will scatter preferentially in the forward direction and will not couple to the lensed optical fiber.

The sample is fabricated on a SOI substrate having a device layer thickness, $t_{dev} = 340$ nm, and buried oxide (BOX) layer thickness, $t_{BOX} = 1\ \mu m$. A 950 K poly (methyl methacrylate) A2 resist is spun onto the sample at 4000 revolutions per minute, and an array of waveguides is patterned via electron beam lithography. After development, the waveguides are defined by dry etching through the device layer. The sample is then cleaved along two perpendicular crystal axes, producing ten SOI TFPRs of different lengths. A scanning electron micrograph of an exemplary device is shown in the inset of Fig. 1.

To characterize the TFPR, 84 fs pulses at 90 MHz repetition rate and centered at $\lambda = 1560$ nm are delivered from a mode-locked erbium-doped fiber laser. The pulses are propagated collinearly with CW radiation from a tunable single

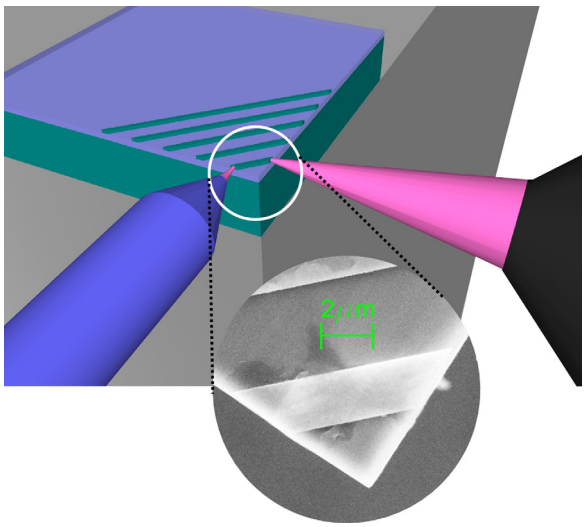

FIG. 1. Schematic depiction of the sample under test and the excitation and detection scheme. A microscope objective (shown on right) couples light into the TFPR and a lensed single mode optical fiber (shown on left), oriented perpendicularly to the angle of excitation, collects the transmitted radiation. A scanning electron micrograph of the $L = 7.80\,\mu$m TFPR is shown in the inset.

mode diode laser ($1509\,\text{nm} \leq \lambda \leq 1581\,\text{nm}$) and are coupled to the TFPR using a 50× microscope objective with a numerical aperture, $NA = 0.85$. The transmitted radiation is collected with a lensed single mode optical fiber and is delivered to an optical spectrum analyzer (OSA). The angle of incidence of the excitation was chosen to be perpendicular to the input facet of the waveguide. A top-view image of scattered radiation from an $L = 31\,\mu$m long TFPR is shown in Fig. 2(a). The optical mode follows a zig-zag pattern as it undergoes multiple total internal reflections at the waveguide sidewalls since the 45° angle of incidence for each reflection exceeds the 20.2° critical angle for total internal reflection. In other words, the radiation is not transmitted by a conventional waveguide mode, but as radiation modes that undergo total internal reflection at the sidewalls. As shown in Fig. 2(b), a distribution of the time-averaged power at the center of the TFPR obtained via finite-difference time-domain (FDTD) simulations exhibits a similar zig-zag trend. Notably, choosing the angle of incidence of the excitation to be normal to the input waveguide end facet results in propagation direction of the waveguide mode to be normally incident on the output facet of the resonator. A reflection coefficient of $R = 0.289$ is calculated from the broadband transmission data from the simulation.

It is essential first to characterize the TFPR wavelength response in the absence of the fs laser pulse excitation (i.e., the passive response). The resonant signature of TFPRs with lengths, $L = \{19.0, 42.7, 66.4\}\,\mu$m are shown in Fig. 3(a). The quality factors, Q, of these resonators are measured to be 340, 888, and 1210, respectively. Shown in Fig. 3(b) is an experimental scan of a resonance of a short ($L = 7.80\,\mu$m) TFPR combined with a calculated wavelength response using the FDTD technique. The Q of this ultracompact TFPR is measured to be 81, while the theoretical value is calculated to be 91. The slight disagreement between the experimental and theoretical Q values is attributed to loss arising from roughness-induced scattering at the TFPR sidewalls. Notably,

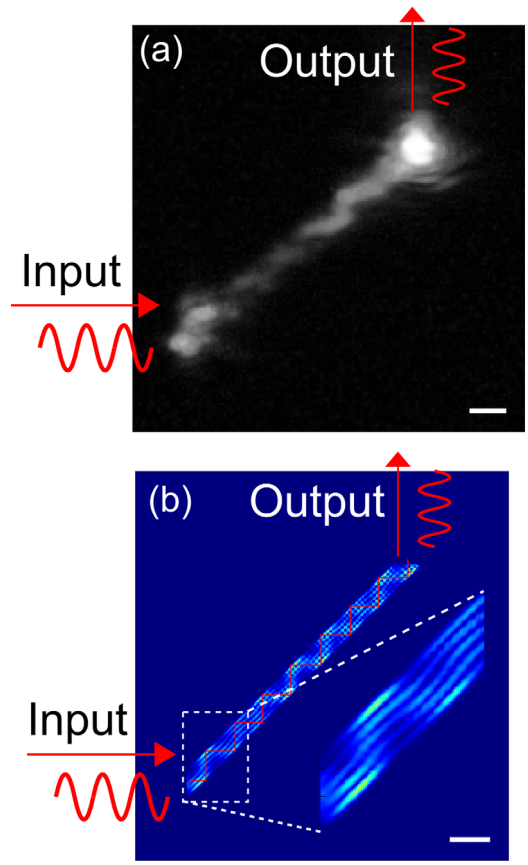

FIG. 2. (a) Top-view image of scattered radiation from the waveguide interfaces following a zig-zag pattern as the mode undergoes total internal reflection at the waveguide interfaces. (b) Time-averaged power distribution in the waveguide obtained by finite-difference time-domain simulations, verifying the multiple total internal reflections as the mode propagates from the input facet to the output. Scale bar is 4 μm for both figures, and the length of the TFPR is $L = 31.1\,\mu$m.

the magnitude of the Q is limited by the short optical path length of the resonator ($n_{eff}L = 42.5\,\mu$m) and the low reflection coefficient of the waveguide end facets ($R = 0.289$).

Femtosecond laser pulses centered at $\lambda = 1560\,\text{nm}$ are used to obtain the power-dependent transmission curve of the $L = 7.80\,\mu$m TFPR, which is shown in Fig. 4(a). Despite the short interaction length within the structure, a transition from the linear transmission regime to the saturation regime is evident. The nonlinear loss arises from both TPA and FCA acting in unison to attenuate the radiation and can be calculated by extrapolating the linear region of the curve and subtracting the measured values from the linear trend. For an input power, $P_{in} = 5.87\,\text{mW}$, approximately, $P_{loss} = 2.86\,\text{mW}$, is lost to TPA and FCA. Input powers less than $P_{in} = 1.0\,\text{mW}$ are insufficient to induce TPA and FCA, and the radiation coupled into the TFPR only undergoes linear losses due to scattering at the waveguide sidewalls.

To demonstrate the influence of ultrafast TPA and FCA on switching operation of the TFPR, the time-resolved dynamics of the nonlinear loss are investigated using a cross-polarized pump-probe technique. Results for two different excitation powers are shown in Fig. 4(b). For the higher excitation power, $P_{in} = 3.42\,\text{mW}$, there are two timescales involved in the interaction. The ultrafast dip in the transmission, which lasts for the duration of the pulse overlap during the scan (~2.28 ps), arises from both TPA and FCA as there is

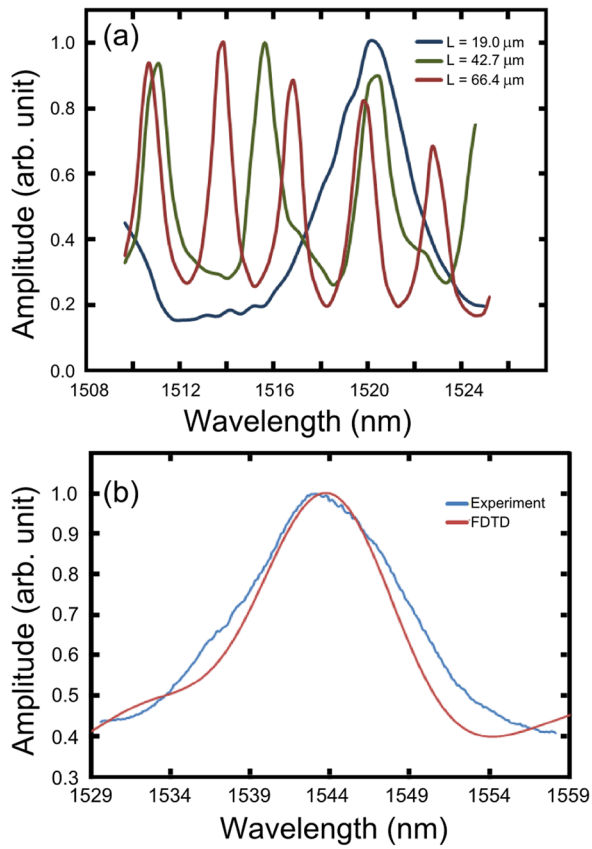

FIG. 3. (a) Experimental broadband transmission of TFPRs with lengths, $L = \{19.0, 42.7, 66.4\}$ μm. The corresponding Q-factors are determined to be 340, 888, and 1210, respectively. (b) Comparison between experimental measurements and calculated results obtained using the FDTD method for the $L = 7.80$ μm TFPR.

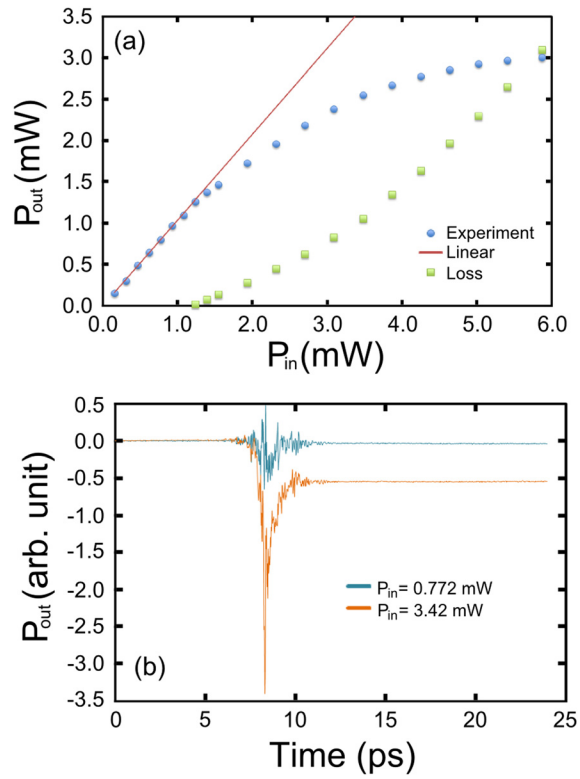

FIG. 4. (a) Measured transmission curve for a TFPR, displaying the linear region and the nonlinear loss region. The linear region is extrapolated, and the experimental values are subtracted from this line to obtain the nonlinear loss. (b) Cross-polarized pump-probe traces for a low input power, $P_{in} = 0.772$ mW and a higher input power, $P_{in} = 3.42$ mW.

significant carrier density to absorb the $\lambda = 1560$ nm photons. The absorption curve recovers over a long time scale of ~225 ps due to direct electron-hole or surface recombination. Interestingly, at a lower excitation power, $P_{in} = 0.772$ mW, only the ultrafast absorption dip corresponding to TPA and FCA is observed, and the long tail associated with free-carrier lifetimes is absent. Previous investigations in III-V semiconductor waveguides have demonstrated that the slow recovery arises from hot electron assisted absorption that is present at high electron densities.[19] For input powers less than approximately $P_{in} = 0.772$ mW, the nonlinear optical interaction is not evident in the pump-probe trace, and only linear interference fringes are visible.

The active tuning of the TFPR is demonstrated by collinearly coupling both the fs laser pulses and the CW radiation into the device. Here, the ultrafast pulses are used to generate free-carriers, which modulate the transmission of the CW radiation. Since the spectra of the fs pulses and the CW radiation overlap, it is necessary to isolate only the induced modulation on the CW radiation. For a single fs laser pulse, the coupled peak power is varied up to a maximum of $P_{in} = 700$ W, and this power is distributed over a wide spectrum (1510 nm $\leq \lambda \leq$ 1610 nm). Conversely, the CW laser diode emits a single mode with a line width, $\Delta\lambda = 20$ pm. An OSA is used as a narrow bandpass filter with $\Delta\lambda = 20$ pm centered at the wavelength of the CW radiation. This scheme effectively filters out 99.996% of the power from the fs laser pulses, and the collected radiation power from the CW laser diode exceeds that from the fs laser pulse, in this same spectral range, by more than an order of magnitude. This technique allows for high resolution spectral sweeps to be performed with the tunable diode with minimal power interference from the fs laser pulse.

By gradually increasing the input fs pulse power and scanning the TFPR spectral response with the tunable CW radiation, it is possible to probe both the loss resulting from TPA and FCA and the change in refractive index, Δn, due to the thermo-optic effect. Free-carriers are produced when high power fs pulses excite the resonator, and thermal energy is deposited in the TFPR as the free-carriers undergo nonradiative recombination. As shown for the $L = 7.80$ μm TFPR in Fig. 5(a), as the power from the fs laser pulse train is increased, the resonant peak response of the TFPR undergoes a red-shift and its amplitude is attenuated. For a low input power, $P_{in} = 1.16$ mW, which is close to the linear regime of the transmission curve in Fig. 4(a), the nonlinear optical interaction is weak, and the resonance is virtually unchanged from the case when only the CW radiation is coupled into the TFPR. For a high coupled power of $P_{in} = 11.3$ mW, the resonant peak is red-shifted by $\Delta\lambda = 7.57$ nm and is attenuated by 66%.

Notably, a plasma effect resulting from the excited free-carriers would give rise to a blue shifted resonance as the refractive index is reduced. While the optical Kerr effect could in principle give rise to a red-shifted resonance peak, it is only present during fs pulse excitation. This effect can be ruled out since the CW radiation probes the time-averaged response of the TFPR. The thermo-optic effect is the only possible effect that would give rise to a red-shift in the resonance that would

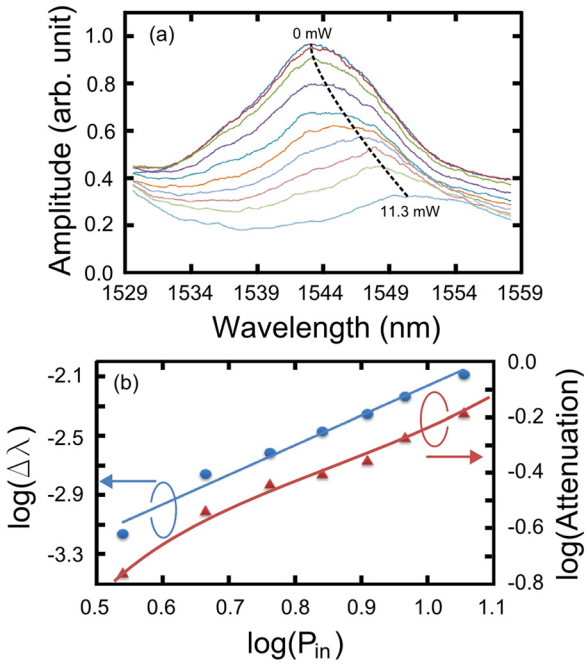

FIG. 5. (a) Broadband transmission spectrum of the resonator as the femtosecond laser power coupled to the device is increased from $P_{in} = 0$ mW to $P_{in} = 11.3$ mW. The power is increased in increments of $\Delta P = 1.16$ mW, with the exception of the highest power, $P_{in} = 11.3$ mW. (b) Log-log plots relating the input power to the wavelength shift and resonance amplitude attenuation. The wavelength shift has a slope of 2.01, while the attenuation does not show a clean linear trend.

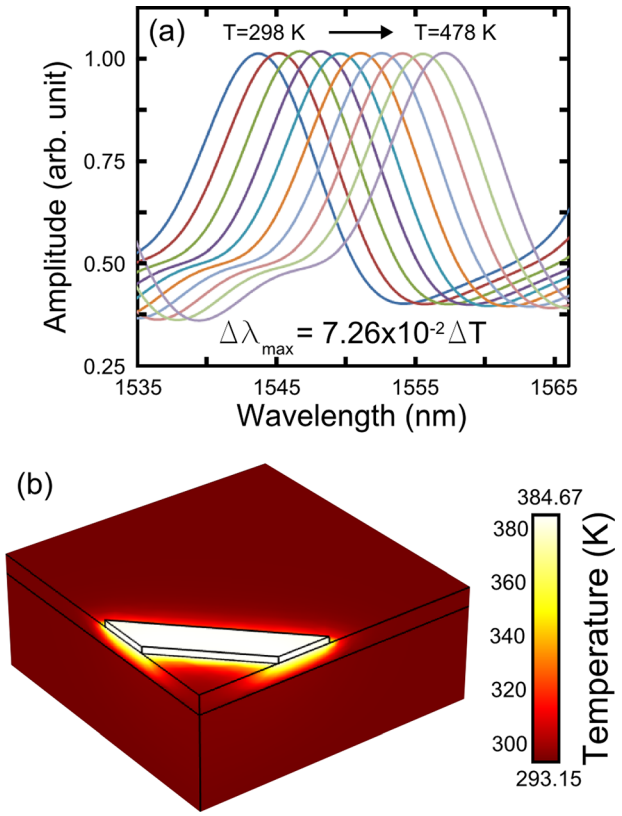

FIG. 6. (a) Broadband transmission spectrum for operating temperatures ranging from $298\,\text{K} \leq T \leq 478\,\text{K}$ in steps of $\Delta T = 20\,\text{K}$, obtained via FDTD simulations. The peak wavelength of the resonance shifts linearly with increasing temperature according to the relation: $\Delta\lambda_{max} = 7.26 \times 10^{-2}\ \Delta T$ [nm]. (b) Temperature distribution for a thermal power of 3 mW distributed uniformly in the TFPR.

be detectable with a CW probe. Previous investigations into the thermal dynamics of SOI waveguide devices determined a response time of $\tau_{thermal} \sim 1\ \mu$s.[20] This is much longer than the period between fs pulses ($T_{pulse} = 11.1$ ns), and we conclude that the temperature of the device is time-invariant.

Log-log plots relating the input power, P_{in}, to the wavelength shift, $\Delta\lambda$, and amplitude attenuation of the resonance are shown in Fig. 5(b). The $\Delta\lambda$ versus P_{in} dependence follows a line of slope of 2.01, demonstrating that $\Delta n \propto P^2{}_{in}$. The $\Delta\lambda$ (where $\Delta\lambda \propto \Delta n$) is, therefore, proportional to the number density of free-carriers excited in the device. This demonstrates that the dominant source of heating is nonradiative recombination of free-carriers and that other factors, such as thermal expansion are negligible. However, the amplitude attenuation does not follow the same dependence, and it is concluded that a combination of the different power-dependencies of TPA and FCA, along with the varying pulse distortion as the TFPR resonance is shifted are responsible for these results.

To gain an understanding of the influence of operating temperature on the resonant characteristics of the TFPR, we perform FDTD simulations on the device. Here, we consider only the effect of temperature and not nonlinear loss mechanisms. An increase in temperature produces an increase in the refractive index via the thermo-optic coefficient, $\Delta n/\Delta T = 1.86 \times 10^{-4}$/K. By varying ΔT systematically, as depicted in Fig. 6(a), we determine the temperature change required to shift the resonant wavelength of the TFPR by $\Delta\lambda$ and observe a linear relation of the form, $\Delta\lambda_{max} = 7.26 \times 10^{-2}\Delta T$. Through these results, we estimate the steady-state temperature of the TFPR to increase by $\Delta T = 104\,\text{K}$ when the input power is $P_{in} = 11.3$ mW. To gain further insight, we perform a thermal stress analysis using COMSOL MULTIPHYSICS to calculate the temperature distribution and the thermal expansion of the device resulting from uniform optical power dissipation. An exemplary temperature distribution for a thermal power of $P_{thermal} = 3.0$ mW is shown in Fig. 6(b), which indicates that the maximum temperature increase in the device is $\Delta T = 91.5\,\text{K}$. The maximum thermal expansion, δx, of any point on the TFPR is calculated to be $\delta x = 0.2$ nm, which is insignificant in altering the TFPR's resonant frequency. By varying the thermal power, we determine its linear influence on the device operating temperature, $\Delta T = 30.5\ P_{thermal}$ [K]. Based on this trend, we estimate that for an input power of $P_{in} = 11.3$ mW, approximately $P_{thermal} = 3.50$ mW remains as a steady-state heat source in the TFPR.

In conclusion, we have investigated the passive resonant characteristics, the ultrafast nonlinear loss mechanisms, and the steady-state temperature change arising from nonradiative recombination of free-carriers in an ultracompact TFPR. By coupling up to $P_{in} = 11.3$ mW from a femtosecond laser into the resonator, the amplitude of the TFPR resonance is attenuated by 65.9% and its spectral position is red-shifted by $\Delta\lambda = 7.57$ nm. It is anticipated that these results will be valuable in the integrated optics community as ultrafast modulators and switches are designed to occupy smaller volumes.

This work was supported by the Natural Sciences and Engineering Research Council of Canada. The authors would like to thank Michael Nielsen for assistance with the COMSOL simulations and Dr. Marco Liscidini for insightful discussions.

[1]R. Soref, IEEE. J. Sel. Top. Quantum Electron. **12**, 1678 (2006).
[2]A. R. Motamedi, A. H. Nejadmalayeri, A. Khilo, F. X. Kärtner, and E. P. Ippen, Opt. Express **20**, 4085 (2012).
[3]R. Dekker, N. Usechak, M. Först, and A. Driessen, J. Phys. D: Appl. Phys. **40**, R249 (2007).
[4]J. A. McCaulley, V. M. Donnelly, M. Vernon, and I. Taha, Phys. Rev. B **49**, 7408 (1994).
[5]R. L. Espinola, M.-C. Tsai, J. T. Yardley, and R. M. Osgood, IEEE. Photon. Technol. Lett. **15**, 1366 (2003).
[6]C. A. Barrios, V. R. Almeida, R. R. Panepucci, B. S. Schmidt, and M. Lipson, IEEE Photon. Technol. Lett. **16**, 506 (2004).
[7]T. Baehr-Jones, M. Hochberg, C. Walker, E. Chan, D. Koshinz, W. Krug, and A. Scherer, J. Lightwave Technol. **23**, 4215 (2005).
[8]T. Chu, H. Yamada, S. Ishida, and Y. Arakawa, Opt. Express **13**, 10109 (2005).
[9]M. W. Pruessner, T. H. Stievater, M. S. Ferraro, and W. S. Rabinovitch, Opt. Express **15**, 7557 (2007).
[10]Z. Jiate, Z. Yong, W. Wanjun, H. Yinlei, Z. Qiang, Y. Jianyi, W. Minghua, and J. Xiaoqing, J. Semicond. **31**, 064009 (2010).
[11]A. Densmore, S. Janz, R. Ma, J. H. Schmid, D.-X. Xu, A. Delâge, J. Lapointe, M. Vachon, and P. Cheben, Opt. Express **17**, 10457 (2009).
[12]Y. Shoji, K. Kintaka, S. Suda, H. Kawashima, T. Hasama, and H. Ishikawa, Opt. Express **18**, 9071 (2010).
[13]H. M. H. Chong and R. M. De La Rue, IEEE Photon. Technol. Lett. **16**, 1528 (2004).
[14]H. K. Tsang, C. S. Wong, T. K. Liang, I. E. Day, S. W. Roberts, A. Harpin, J. Drake, and M. Asghari, Appl. Phys. Lett. **80**(3), 416–418 (2002).
[15]M. Dinu, F. Quochi, and H. Garcia, Appl. Phys. Lett. **82**(18), 2954–2956 (2003).
[16]D. J. Moss, L. Fu, I. Littler, and B. J. Eggleton, Electron. Lett. **41**(6), 320–321 (2005).
[17]T. Liang, L. Nunes, T. Sakamoto, K. Sasagawa, T. Kawanishi, M. Tsuchiya, G. Priem, D. van Thourhout, P. Dumon, R. Baets, and H. Tsang, Opt. Express **13**(19), 7298–7303 (2005).
[18]T. K. Liang, L. R. Nunes, M. Tsuchiya, K. S. Abedin, T. Miyazaki, D. van Thourhout, W. Bogaerts, P. Dumon, R. Baets, and H. K. Tsang, Opt. Commun. **265**(1), 171–174 (2006).
[19]H. K. Tsang, P. A. Snow, I. E. Day, I. H. White, R. V. Penty, R. S. Grant, Z. Su, G. T. Kennedy, and W. Sibbett, Appl. Phys. Lett. **62**, 1451–1453 (1993).
[20]F. Magno, F. Dell'Olio, and V. M. N. Passaro, *Proceedings of the* COMSOL *Users Conference* (Milano, Italy, 2006).